High-performance polyamides with engineered disorder

Nicolas Candau, Sylvain Galland, Julien Cretenoud, Sandor Balog, Véronique Michaud, Jean-Marc Chenal, O. Lame, Christopher J. G. Plummer, Holger Frauenrath

Enhanced Ductility in High Performance Polyamides due to Strain-Induced Phase Transitions

Nicolas Candau,[1]* Jean-Marc Chenal,[2] Olivier Lame,[2] Pascal Schouwink,[3] Véronique Michaud,[4] Christopher J.G. Plummer,[1]* Holger Frauenrath[1]

[1] Laboratory of Macromolecular and Organic Materials (LMOM), Institute of Materials (IMX), Ecole Polytechnique Fédérale de Lausanne (EPFL), Station 12, CH-1015 Lausanne, Switzerland.

[2] Université de Lyon, INSA de Lyon, MATEIS, CNRS, UMR 5510, 69621 Villeurbanne, France.

[3] ISIC Valais, École Polytechnique Fédérale de Lausanne (EPFL), Rue de l'industrie 17, CH-1951 Sion, Switzerland.

[4] Laboratory for Processing of Advanced Composites (LPAC), Institute of Materials (IMX), Ecole Polytechnique Fédérale de Lausanne (EPFL), Station 12, CH-1015 Lausanne, Switzerland.

* Corresponding authors:

christopher.plummer@epfl.ch

nico.candau@gmail.com

Abstract

Copolymerizing poly(hexamethylene terephthalamide-*co*-isophthalamide) (PA6TI) with 40 *wt*% polyamide 66 (PA66) results in only minor decreases in modulus and yield stress owing to isomorphous substitution of PA6TI units by PA66 units in the PA6TI α phase, so that crystallinity is maintained in the resulting PA6TI-66 terpolymer. However, the ductility also significantly increases. This is attributed to a deformation-induced transformation of the PA6TI α phase to a disordered form of the PA66 α phase, where PA6TI units constitute defects and the chains adopt extended conformations. This phase is argued to be favored in initially amorphous PA66-rich regions and hence stabilizes interlamellar micro-necks that develop during yielding. By contrast, segregation of isophthaloyl units to the amorphous regions in PA6TI hinders strain-induced crystallization, leading to failure at significantly lower strains. Brittleness may therefore be a generic problem when comonomers are used to facilitate processing, but one that may be overcome through proper microstructural control.

Introduction

An outstanding challenge in developing new technical thermoplastic polymers and composites for the replacement of metals in structural and semi-structural applications is to achieve high strength and stiffness without compromising ductility and toughness [1,2]. The tensile ductility of thermoplastic polymers and hence their ability to absorb energy during fracture generally depends on the competition between homogeneous plastic deformation and damage resulting from the formation, growth, and coalescence of internal voids [3-8]. Increasing the yield stress and hence the effective strength of a thermoplastic without modifying the threshold for damage development therefore tends to shift the balance towards a more brittle response [9].

In lamellar semicrystalline polymers deformed in tension, voiding is typically associated with the amorphous interlamellar layers, which may be in the glassy or rubbery state depending on the type of polymer and the test conditions, and localized lamellar break-up in regions where the lamellar trajectories are oriented close to the tensile axis. Voiding is therefore favored when the plastic resistance of the crystalline lamellae is high, resulting in localization of deformation to the amorphous phase and a consequent build-up of triaxial stresses owing to confinement by the lamellae [3,4]. Relaxation of these triaxial stresses after voiding facilitates both continued deformation of the amorphous regions and shear of the crystalline lamellae. It follows that void formation is frequently associated with macroscopic yielding, although cooperative shear deformation of the amorphous and crystalline phases may take place without extensive void initiation and growth if the plastic resistance is sufficiently low [3,4,10]. Deformation beyond the yield strain then results in a transformation from a lamellar structure to a fibrillar structure, characterized by a high degree of molecular orientation in the draw direction. This transformation involves extensive shear, fragmentation and unfolding of the original lamellae, further relaxing the constraints on void growth and coalescence in tension [3,4,10-13].

The extent to which these mechanisms develop in a highly voided semicrystalline polymer prior to macroscopic failure depends on the mechanical stability of the ligaments that separate the voids, and the relaxation of local deformation-induced stress concentrations through crystal slip and related processes. Competition between ductile and brittle behavior is therefore sensitive to both internal variables such as

the degree of crystallinity and lamellar thickness, the presence of local structural or microstructural defects, the molar mass, the entanglement density and the architecture of the polymer chains, and external variables, such as strain rate and temperature, through their influence on the relaxation behavior of the crystalline lamellae and amorphous regions, particularly if these latter are in the glassy state [3,12,14-18].

Semicrystalline semiaromatic polyamides are a particularly promising class of high-performance thermoplastics that combine molecular rigidity with intermolecular hydrogen bonding to give yield stresses that may exceed 100 MPa in the dry state and hence effective specific tensile strengths that rival those of many metals. However, they also typically show a macroscopically brittle or semi-brittle response in tension at room temperature [19,20]. Reducing the lamellar thickness and/or the degree of crystallinity by modifying the processing conditions may improve the ductility of polyamides, but is accompanied by a loss in yield strength and stiffness [21,22]. This is also true of traditional "rubber toughening" strategies, in which highly dispersed soft inclusions promote ductility through mechanisms such as local constraint release or delocalization of crack-tip microdeformation [23-25]. There has been some effort to reproduce these effects in polyamides using rigid inorganic particles that reinforce their stiffness, but this has so far proven to be ineffective for intrinsically brittle matrices [26].

Another potential way to improve ductility without sacrificing stiffness is to promote the formation of a phase whose lamellae show reduced plastic resistance but can transform to a more mechanically resistant phase during deformation. Certain processing conditions favor the mesomorphic β phase in polyamide 6 (PA6), for example [27,28], which undergoes a strain-induced transformation to the stable α phase, resulting in self-reinforcement and significantly higher strains to failure than in specimens in which the α phase is the majority crystalline phase prior to deformation [29]. Improvements in ductility have also been obtained in isotactic polypropylene (iPP) containing stereo-defects that promote the formation of disordered γ phase lamellae, which transform to either a pseudo-hexagonal mesophase or the α phase at large deformations [30-33]. These results imply that it may also be possible to improve the ductility of semicrystalline semiaromatic polyamides by tailoring microstructural order and disorder to promote suitable polymorphism.

The present work stems from our efforts to improve the tensile ductility of a commercial high-yield stress, high-modulus semicrystalline semiaromatic random copolyamide, poly(hexamethylene terephthalamide-

co-isophthalamide) (PA6TI), containing a 2:1 ratio of terephthaloyl (T) to isophthaloyl (I) units, without significantly compromising its strength and stiffness. Our approach is to randomly insert controlled concentrations of selected aliphatic defects into the PA6TI chains. This is conveniently carried out by reactive compounding with a suitable aliphatic polyamide, taking advantage of the tendency of compatible polyamide blends to undergo rapid and extensive transamidation in the melt state without substantial changes in molar mass [34]. We have shown previously that substitution of the T or I units of PA6TI with adipoyl or sebacoyl units by high temperature melt compounding with up to 40 *wt*% poly(hexamethylene adipamide) (PA66) or poly(hexamethylene sebacamide) (PA610), results in random copolyamides that exhibit only minor changes in the degree of crystallinity, morphology and overall crystalline structure, owing to the ability of these aliphatic comonomers to at least partly conform to the crystal structure characteristic of the unmodified PA6TI [34,35]. The room temperature stiffness, as reflected by the tensile moduli of the resulting random terpolymers PA6TI-PA66 and PA6TI-PA610, therefore remains comparable to that of PA6TI, and there are only modest reductions in yield stress. At the same time, however, there is a large increase in the room temperature strain to failure in uniaxial tension, which may even exceed that of the aliphatic homopolymers PA66 and PA610 despite the lower yield stress of these latter. This is suggested to be due to the ability of the aliphatic units in the aliphatic-rich amorphous regions in the PA6TI-PA66 and PA6TI-PA610 terpolymers to co-crystallize with the aromatic units to form a distinct phase on yielding [35].

Here, we report the results of a study of the tensile deformation behavior of PA6TI, PA66 and the random terpolymer of PA6TI containing 40 *wt*% PA66, henceforth referred to as PA6TI-66, with emphasis on the role of thermomechanical transitions and volumetric deformation over an extended range of test conditions, and the evolution of the crystallographic texture as a function of tensile strain in specimens tested at ambient temperature. We correlated the macroscopic stress-strain behavior with the phase behavior and the extent of void formation and/or growth as reflected by the volumetric strain, in order to establish a direct link between the chain microstructure and the improved ductility of the terpolymer. Our results strongly indicated that deformation-induced crystallization in PA6TI-66 serves to both stabilize the ligaments separating the voids characteristic of post-yield deformation and relax local stresses in the deformed material. They hence provide pointers to new improved strategies for property optimization in high-performance thermoplastic polymer materials.

Results and Discussion

In assessing the competition between ductile and brittle behavior in glassy semicrystalline thermoplastics, it is important from the outset to consider their behavior over a wide range of conditions in the light of not only their morphology and structure, but also the thermal and thermomechanical transitions associated with the crystalline and the amorphous phases. These transitions may have a profound influence on yielding, which is typically sensitive to the proximity of the test temperature to the glass transition temperature, T_g, or any secondary relaxations below T_g. For example, selective plasticization of the glassy amorphous phase owing to moisture uptake in glassy aliphatic polyamides such as PA66 is well known to lead to significant decreases in the yield stress [36]. It is therefore essential when comparing the mechanical response of different polyamides to work under conditions of controlled humidity or, as in the present case, with specimens that have been carefully dried prior to testing.

The glass transition temperatures, T_g, of dried as-molded specimens of PA6TI, PA6TI-66 and PA66 were determined from differential scanning calorimetry (DSC) heating scans at 10 °C/min to be 58, 86, and 135 °C for PA66, PA6TI-66 and PA6TI, respectively, and the temperatures of the corresponding melting peaks, T_m, were 260, 275, and 310 °C (Figure 1a). 1D-Wide-angle X-ray diffraction (1D-WAXD) at different temperatures confirmed the PA66 moldings to show the usual room temperature triclinic α crystal modification (a = 4.9 Å, b = 5.4 Å, c = 17.2 Å, α =48.5 °, β = 77 °, γ = 63.5 ° [37]), which transformed to the high-temperature pseudo-hexagonal α' modification as the temperature increased (Figure 1b). The corresponding Brill transition temperature [38,39], marked by the convergence of the (100) and (010)/(110) spacings (4.4 and 3.7 Å respectively at room temperature) was approximately 200 °C. As demonstrated previously by WAXD and selected area electron diffraction (SEAD), the dominant crystalline phase of PA6TI-66 was similar to that of the PA6TI α-modification (a = 5.03 Å, b = 5.33 Å, c = 16.42 Å, α = 50.5 °, β = 79.0 °, γ = 94.0 ° [35]) with only minor differences in the positions and intensities of the main reflections. However, whereas the PA6TI d-spacings changed little with temperature throughout the range investigated, the PA6TI-66 (010) spacing, that is, the spacing of the stacked hydrogen-bonded sheets associated with the α-modification, increased from 3.95 to 4.2 Å as the temperature increased from room temperature to 200 °C. The PA6TI-66 (010) spacing and the main PA66 $hk0$ spacings hence became very close at the PA66 Brill transition, and remained close up to the T_m of PA66 of about 260 °C.

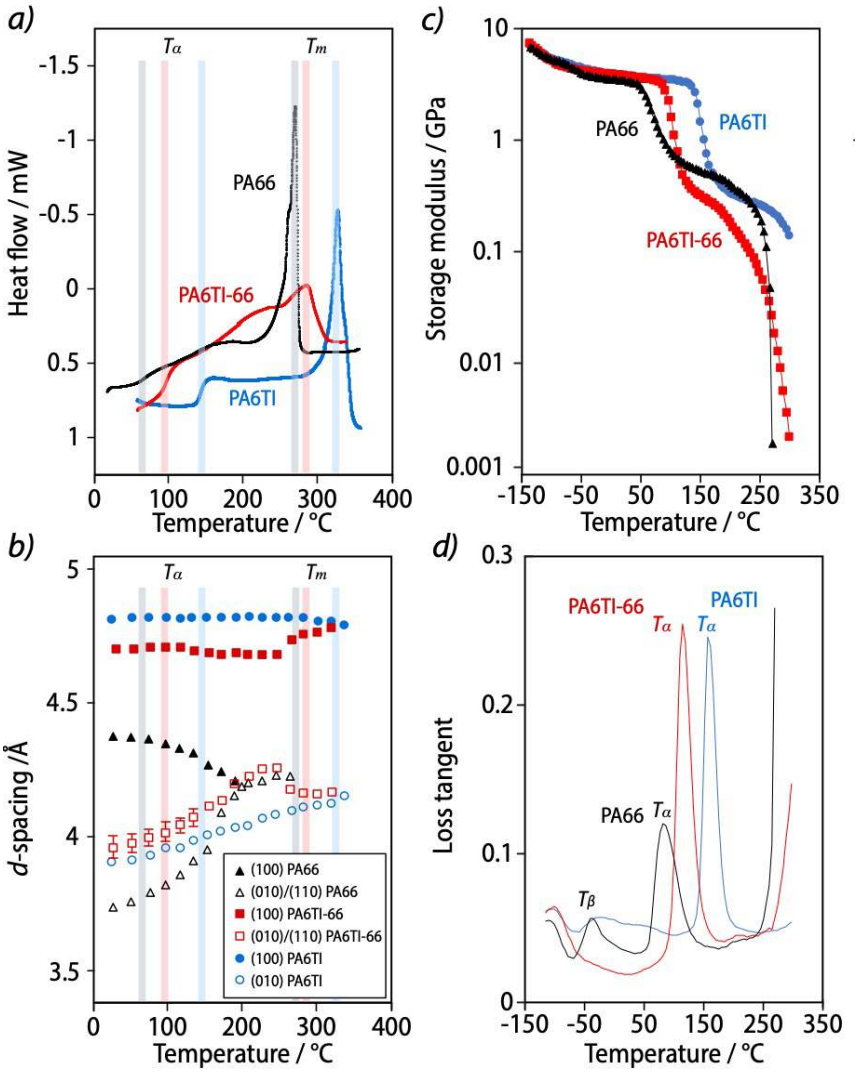

Figure 1. *a)* DSC heating scans at 10 °C/min from the as-molded materials, showing the glass transition temperature, T_g, and melting point, T_m, in each case. *b)* d-spacings corresponding to the main Bragg peaks in the different materials determined by wide-angle X-ray diffraction (WAXD) as a function of temperature. *c)* Storage modulus, E', and *d)* loss tangent, tan δ, from DMA heating scans in tension at a frequency of 1 Hz with a maximum strain of 0.001.

At still higher temperatures, where PA66 became fully amorphous, the d-spacings of the remaining crystalline material in PA6TI-66 converged once more with those observed for the unmodified PA6TI, and residual crystallinity persisted up to temperatures well beyond the nominal T_m of PA6TI-66 of 275 °C (Figure 1b, Supplementary Figure S1).

Because the Brill transition in aliphatic polyamides is associated with conformational motion of the aliphatic segments [40-42], we attributed the greater temperature sensitivity of the PA6TI-66 d-spacings with respect to that of the PA6TI d-spacings to the significantly higher aliphatic content of the PA6TI-66

crystalline phase, up to 20 % of the T units being substituted by adipoyl units [35]. It was also inferred from the very broad melting range of PA6TI-66 (Figure 1a) that its local composition, order, and lamellar thicknesses varied significantly, and that there may also have been substantial reorganization of its lamellar structure during heating. However, regardless of the extent of polymorphism at high temperatures, the crystal structures in all the materials in the undeformed state changed little with temperature at $T < T_g$.

Dynamic mechanical analysis (DMA) was then used to correlate the observed thermal transitions with the low-strain mechanical response as well as highlight any additional thermomechanical relaxations below T_g (Figure 1c,d). The α transition temperatures, T_α, associated with the tan δ peaks observed in the glass transition zone in DMA heating scans at 1 Hz, were 70, 105 and 150 °C for PA66, PA6TI-66 and PA6TI, respectively.

The strong β relaxation at about −50 °C in PA66 was less prominent in the dry PA6TI-66 and PA6TI specimens [43,44]. However, all the materials showed a clear γ relaxation below −100 °C, which is generally attributed to local motion of the methylene segments [43-47]. A plateau in the storage modulus, E', was observed at $T > T_\alpha$, which was associated with somewhat higher values of E' in PA66 than in PA6TI and PA6TI-66. A possible explanation for this is that the degree of crystallinity, χ, estimated from small-angle X-ray scattering (SAXS) for PA66 injection moldings produced under the same conditions as in the present work was 29 *vol*%, as opposed to 23 *vol*% for PA6TI, and 25 *vol*% for PA6TI-66 [35]. E' then decreased sharply in PA66 and PA6TI as the temperature approached their respective T_m, while the decrease in E' associated with melting in PA6TI-66 was more gradual, consistent with its broader melting range (Figure 1b).

In conclusion, consistent thermomechanical behavior was observed at small deformations in PA6TI and PA6TI-66 in the glassy state between −100 °C and T_g. More importantly, no major secondary relaxations were observed in either material in this temperature range, despite the increased aliphatic content of the amorphous phase in PA6TI-66.

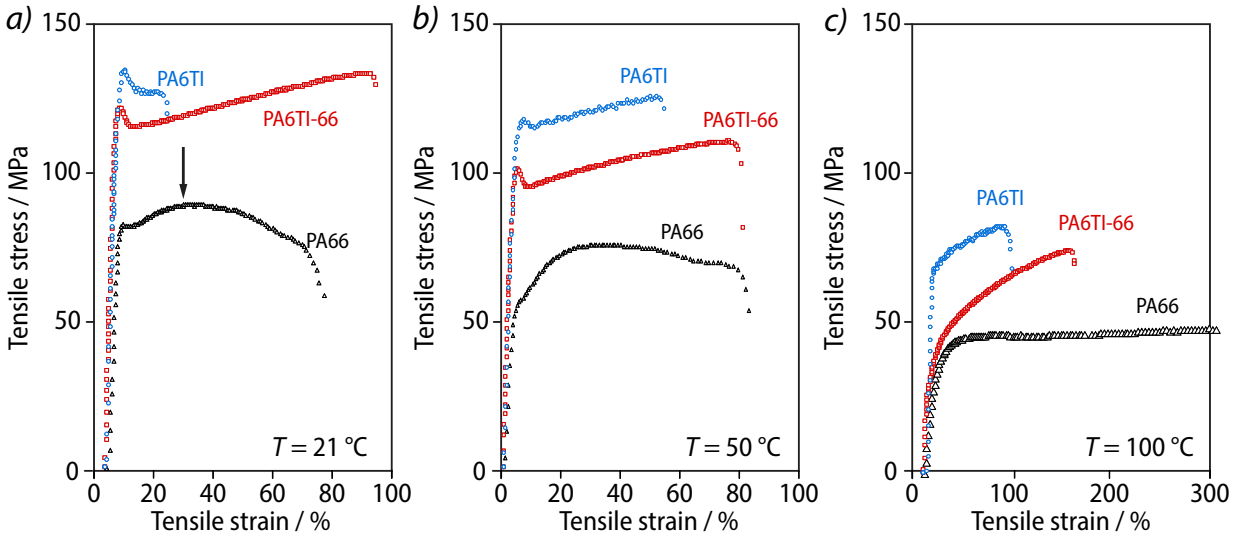

Figure 2. Representative nominal stress-strain curves from uniaxial tensile tests performed at a strain rate of 0.05 min^{-1} and *a)* 21 °C, *b)* 50 °C and *c)* 100 °C on dry injection moldings of PA66 (blue), PA6TI (black) and PA6TI-66 (red), as shown. The arrow in *a)* indicates the second yield point in PA66.

The influence of thermomechanical relaxations on the large strain behavior is reflected by not only the viscoelastic response, but also plastic yielding and/or ultimate failure. At temperatures well below T_α, the nominal tensile stress-strain curves for all the materials showed a well-defined nominal yield stress, σ_y, which was associated with a clear yield-drop (Figure 2). However, at temperatures close to and above T_α, the stress-strain curves became highly non-linear at low nominal axial strains, ε, and the nominal stress, σ, increased monotonically during yielding so that a distinct yield point could no longer be identified. The nominal yield stress, σ_y, was therefore defined under these conditions as the intercept of the tangent to the stress-strain curve at zero strain to the tangent of the stress-strain curve at 50 % strain. In regimes where PA6TI and PA6TI-66 showed both a yield-drop and significant ductility, post-yield strain hardening was observed for ε up to close to the nominal strain to failure, ε_f. By contrast, at $T < T_\alpha$, the stress-strain curves for PA66 reflected the double yielding behavior typical of dry specimens of this and other similar aliphatic polyamides, an initial weak yield-drop being followed by a second broad maximum in σ at higher ε, beyond which σ gradually decreased as ε approached ε_f [48,49].

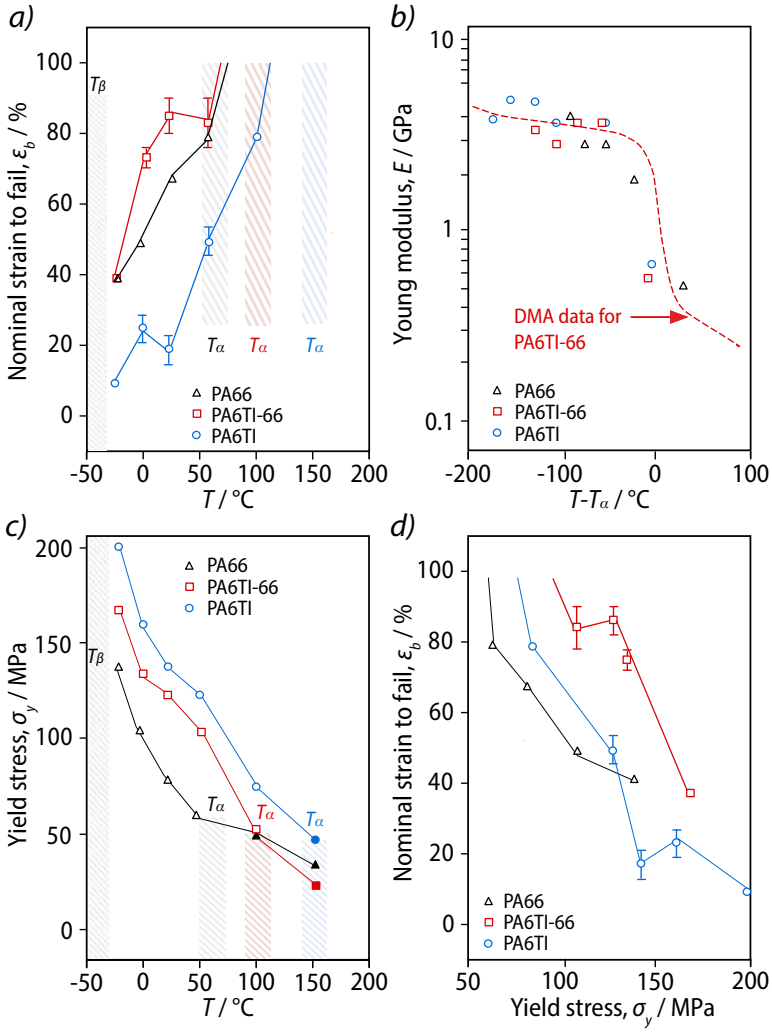

Figure 3. *a)* The average nominal tensile strain to failure, ε_f, for the different materials as a function of temperature, T (all the materials became fully ductile at temperatures above T_α, with ε_f reaching 200–300 %). *b)* Young's modulus, E, estimated from tensile stress-strain curves for the different materials at T close to T_α expressed as a function of $T - T_\alpha$, along with DMA data for PA6TI-66 for comparison. *c)* Nominal tensile yield stress, σ_y, as a function of T (the filled symbols correspond to data for which there was no distinct yield point and σ_y was defined as the intercept of the tangent to the stress-strain curve at zero strain to the tangent of the stress-strain curve at 50 % strain). *d)* ε_f as a function of σ_y at temperatures below T_α.

Direct comparison of the temperature dependence of the strain to failure, Young's modulus, and yield stress for the different materials (Figure 3) confirmed the importance of the α transition for the large strain behavior, but also revealed significant additional features. Most strikingly, as observed previously in room temperature measurements [35], the strain to failure, ε_f, of the terpolyamide PA6TI-66 was substantially higher than of PA6TI at $T < T_\alpha$, and indeed it was even higher than that of PA66 (Figure 3a), although its Young's modulus, E, remained comparable to that of PA6TI, consistent with the DMA data for E' (Figure 3b).

Moreover, the yield stress, σ_y, of PA6TI-66 was only some 10–15 % less than that of PA6TI at any given temperature (Figure 3c). The yield stresses of PA6TI and PA6TI-66 also showed a slight plateau between about 0 and 50 °C. However, the yield stress of PA66 fell steeply with increasing temperature in the same regime, owing to its stronger β relaxation as well as the proximity of its α relaxation. Hence, PA6TI-66 showed a consistently higher strain to failure, ε_f, than any of the other materials for any given value of σ_y at test temperatures $T < T_\alpha$ (Figure 3d). This is a strong indication that the improved room temperature ductility of PA6TI-66 with respect to that of PA6TI was a consequence not only of its lower T_g and the concomitant reduction in σ_y, but also a significantly greater load-bearing capacity with respect to σ_y at large deformations, which are expected to be characterized by significant irreversible damage accumulation.

In order to gain further insight into the differences in the strain to failure, ε_f, in the different materials at $T < T_\alpha$, we therefore monitored the local volumetric strains, ε_v, associated with yielding and subsequent drawing [50,51]. The local volumetric strain is expected to reflect void nucleation, growth, and coalescence via deformation and break-down of the ligaments separating the voids, which leads ultimately to macroscopic failure. These phenomena have been extensively described using continuum damage models and the mechanics of porous media approach [52], exemplified by the Gurson-Tvergaard-Needleman (GTN) model, in which the damage parameter is the void volume fraction [53]. When modified to account for the viscoelastic, viscoplastic, and strain hardening behavior of the multicomponent polymer matrix [54-57], such models have been shown to provide an accurate phenomenological description of the evolution of the local void content and morphology in bulk specimens of spherulitic semicrystalline aliphatic polyamides under a variety of loading conditions [56-58].

We determined the local volumetric strains by using digital image correlation (DIC) to measure the axial and transverse strain fields at the specimen surface during uniaxial deformation (Figure 4, Supplementary Figure S2). Assuming transverse isotropy, the volumetric strain $\varepsilon_v = \varepsilon_1 + 2\varepsilon_2$, where ε_1 and ε_2 are the local axial strain and lateral strain, respectively. In the low-strain linear elastic regime, in which ε_1 was approximately uniform and equal to ε along the entire gauge length of the specimens, the measured ε_v (Figure 4d,e,f) were consistent with the elastic dilation, $\varepsilon_v^{el} = (1 - 2\nu)\sigma/E$, taking the Poisson's ratio, ν, to be 0.39, which is typical of glassy semicrystalline polyamides [59].

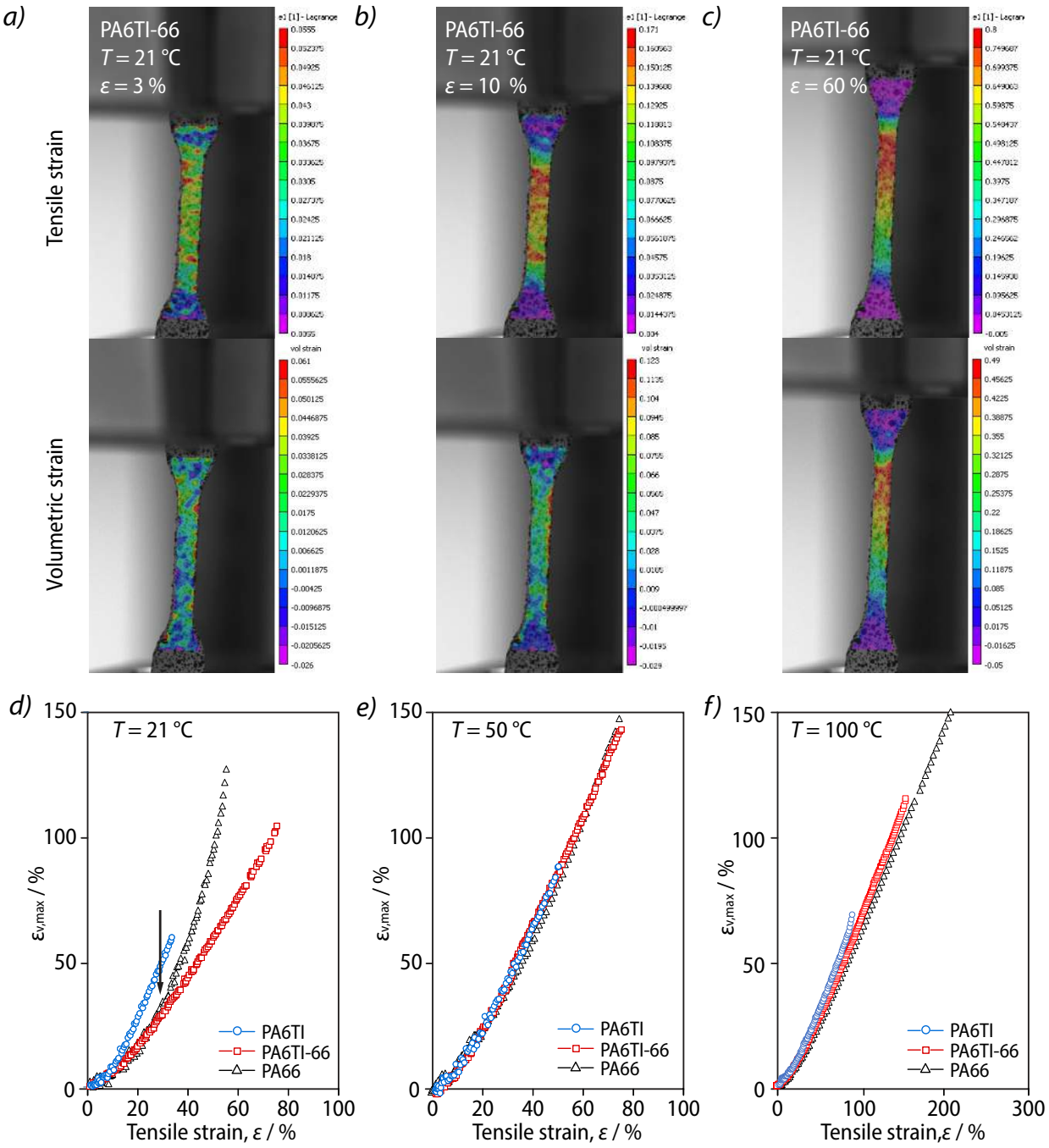

Figure 4. Axial and volumetric strain fields of PA6TI-66 deformed at ambient temperature at a strain rate of 5 % min^{-1} and recorded at macroscopic strains of *a)* 3 %, *b)* 10 % and *c)* 60 %. Maximum volumetric strains, ε_{vmax}, estimated from the local longitudinal, ε_1, and transverse strains, ε_2, measured by digital image correlation (DIC) in uniaxial tensile tests performed at a strain rate of 0.05 min^{-1} and *d)* 21 °C, *e)* 50 °C and *f)* 100 °C on dry injection moldings of PA66, PA6TI and PA6TI-66. The arrow in *d)* indicates the strain corresponding to the second yield point in PA66.

At $T < T_\alpha$, yielding in all materials was characterized by the development of diffuse maxima in ε_1 along the length of the specimen rather than formation of a sharp neck (Figure 4a–c). For the purpose of the following

discussion, therefore, a "maximum volumetric strain", $\varepsilon_{v\max}$, was defined as the mean value of ε_v in regions in which ε_1 reached at least 80 % of its maximum measured value along the specimen (see the Supplementary Information). The absolute values of ε_{vmax} defined in this way were consistent with the results of previous investigations into aliphatic polyamides using similar experimental techniques [60], and greatly exceeded ε_v^{el} ($\lesssim$ 1 % depending on σ_y) as ε increased beyond the yield strain (Figure 4d,e,f). This indicated formation and growth of internal voids and/or the growth of pre-existing voids to play an important role in yielding and plastic deformation, regardless of the aromatic content.

The rate of change of ε_{vmax} with respect to the overall nominal strain, $d\varepsilon_{v\max}/d\varepsilon$, provides a measure of the rate of damage accumulation. At room temperature, $d\varepsilon_{v\max}/d\varepsilon$ was similar in PA6TI, PA6TI-66 and PA66 immediately above the yield strain (Figure 4d). However, it accelerated sharply in PA6TI at $\varepsilon \approx 10$ %, and this acceleration was closely followed by macroscopic failure associated with the appearance of highly localized crack-like zones of intense stress-whitening. We observed a similar acceleration in $d\varepsilon_{v\max}/d\varepsilon$ with increasing ε in PA66 at $\varepsilon \approx 25$ % during room temperature deformation (Figure 4d, arrow), which was in this case identified with the onset of strain softening beyond the second yield point (Figure 2a, arrow) as ε increased further towards the strain to failure, ε_f, of about 70 %. By contrast, $d\varepsilon_{v\max}/d\varepsilon$ was roughly constant in PA6TI-66 up to its ε_f of about 80 %, so that $\varepsilon_{v\max}$ reached values more than four times greater than in PA6TI despite the comparable nominal stress levels at failure in the two materials. These results provided a clear demonstration of the improved stability of the terpolymer PA6TI-66 with respect to internal voiding at large strains, consistent with its enhanced ductility.

As T increased towards T_α, the post-yield values of $d\varepsilon_{v\max}/d\varepsilon$ remained comparable to those seen at 21 °C (Figure 4e), albeit without the marked acceleration prior to failure that characterized the room temperature response of PA6TI and PA66. Indeed, large $\varepsilon_{v\max}$, implying extensive internal void formation, were observed even at $T \gtrsim T_\alpha$, where ε_1 became increasingly uniform along the gauge length and all the materials were highly ductile (Figure 4f). However, the ε_{vmax} associated with failure remained higher in PA6TI-66 than in PA6TI, implying the mechanical stability of the voided material in PA6TI-66 to be greater than in PA6TI over the whole temperature range $T \gtrsim T_\alpha$,.

To investigate the microscopic origins of the voids, local tensile deformation mechanisms were imaged by transmission electron microscopy (TEM) of roughly 300 nm thick sections of the different polymers

prepared from the bulk moldings with an ultramicrotome. Prior to deformation, the sections were recrystallized by cooling from the melt at 10 K/min under nitrogen, resulting in a two-dimensional spherulitic texture with spherulite diameters of the order of 2 μm. The sections were mounted on copper grids and deformed in uniaxial tension at room temperature to a maximum nominal strain of about 50 % [61]. In each case, flame-shaped shear deformation zones propagated from stress concentrations, such as dust particles or large voids, and were accompanied by more diffuse shear in the rest of the films (Figure 5). The main deformation zones showed well-developed fibrillar textures in PA6TI-66 and PA66, associated with local axial strains of more than 200 % as estimated from the mass thickness contrast of the TEM images [62]. As observed previously in glassy aliphatic polyamides, these fibrillar deformation zones were characterized by fragmentation of the original lamellae, which tended to initiate in the equatorial and meridional sectors of the spherulites in the early stages of deformation [4,63-66]. By contrast, the PA6TI films broke down at much lower strains, consistent with the behavior observed in the bulk tensile tests, and the corresponding deformation zones contained partly deformed spherulites rather than fully fibrillar structures. Interlamellar voiding was nevertheless still present in the PA6TI films in the early stages of deformation.

These results suggested that the more ductile behavior of PA6TI-66 was due to an increase in the load-bearing capacity of the nanoscopic ligaments between interlamellar voids. Although improvements in the stability of such ligaments are often attributed to a higher molar mass and/or a greater entanglement density, in the present case the weight-average molar masses, M_w, of all the polymers were in the range 25’000–32’000 g/mol after extrusion compounding [34], which was significantly greater than the respective entanglement molar masses, M_e, of 1’700 in PA66 and 2’800 g/mol in PA6TI [67,68]. To account for the observed differences in ductility, we therefore focused on the crystallographic texture and its evolution as a function of ε during tensile deformation as determined from small-angle X-ray scattering (SAXS) and wide-angle X-ray diffraction (WAXD) measurements performed *in situ* during tensile testing.

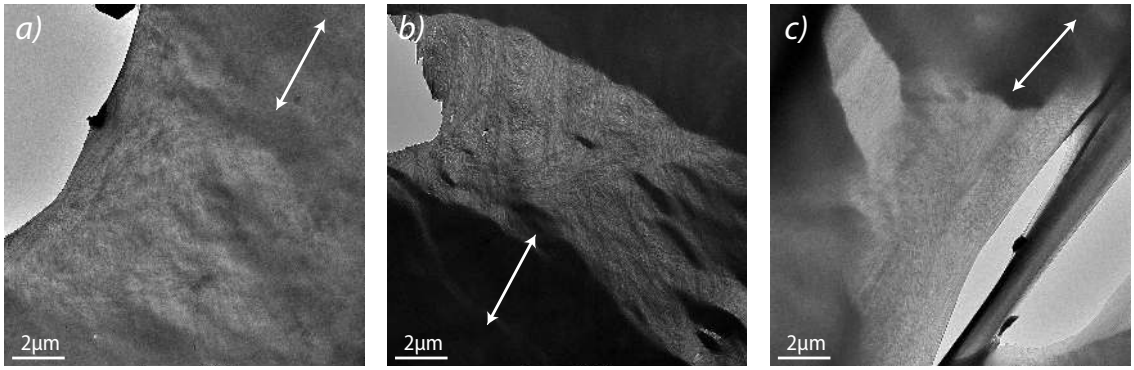

Figure 5. TEM images of fibrillar deformation zones propagating from defects in approximately 300 nm thick films of *a)* PA6TI, *b)* PA6TI-66 and *c)* PA66. The arrows indicate the strain direction in each case.

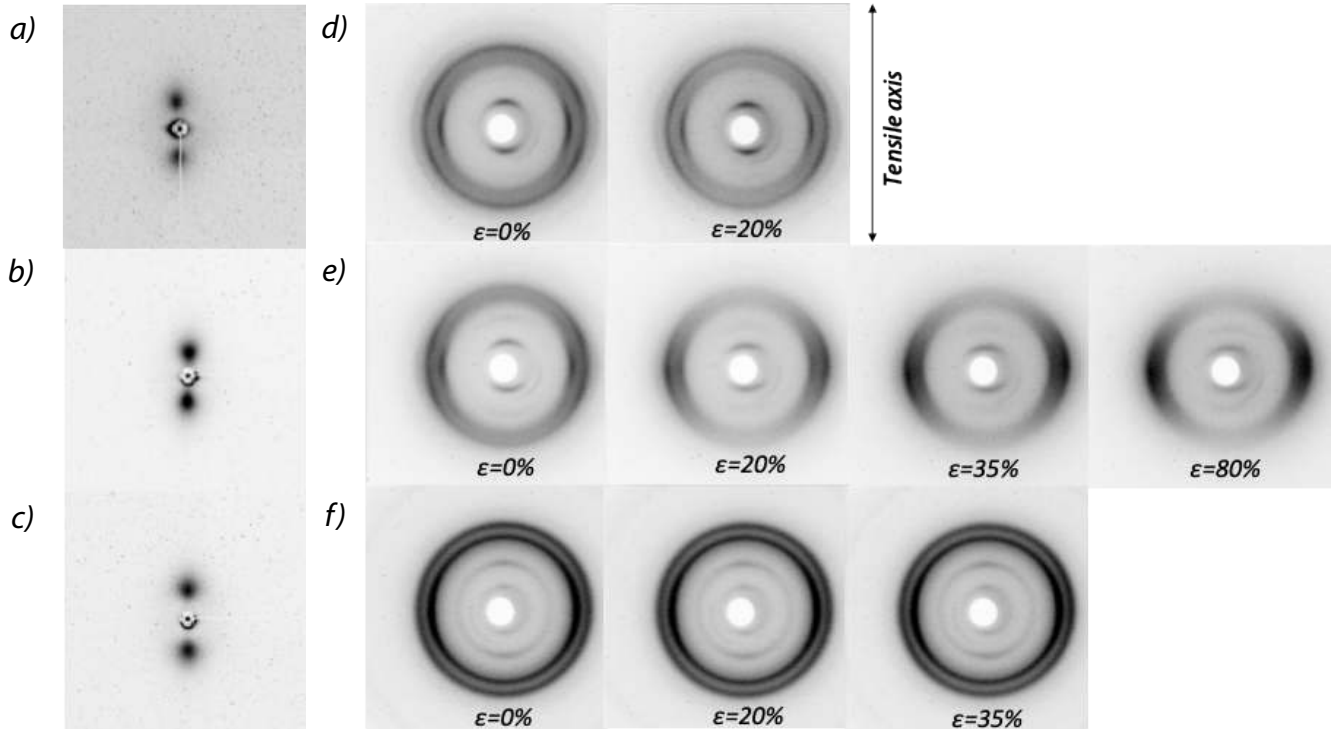

Figure 6. 2D-SAXS patterns from *a)* PA6TI, *b)* PA6TI-66, and *c)* PA66 obtained in transmission mode from undeformed specimens (specimen axis vertical). The positions of the symmetric diffuse peaks due to alternating stacks of crystalline and amorphous lamellae indicated significant orientation of lamellar trajectories normal to the specimen axes, and hence significant molecular orientation along the injection direction in all the materials. 2D-WAXD patterns from *d)* PA6TI, *e)* PA6TI-66, and *f)* PA66 obtained in transmission mode in the undeformed state and *in situ* at the nominal tensile strains indicated (specimen/tensile axis vertical). The diffuse asymmetric reflections at Bragg angles of about 10 ° in the bottom left-hand quadrant in *a)* and *b)* and in the bottom right-hand quadrant in *c)* are artefacts due to diffusion from a Kapton window placed at the end of the X-ray tube.

2D-SAXS patterns of undeformed specimens showed there to be significant orientation of the planes of the crystalline lamellae perpendicular to the axes of the injection moldings (Figure 6a–c, Supplementary Figure S3), with lamellar long periods, L, of approximately 8.7, 8.8 and 6.6 nm in PA6TI, PA6TI-66 and PA66, respectively, which were comparable to previously reported values for injection moldings processed under the same conditions [35]. Lamellar separation and interlamellar voiding were therefore expected to play an important role in the early stages of irreversible tensile deformation along the specimen axes, assuming the local stress to be roughly uniform and perpendicular to the lamellar trajectories, consistent with the large observed volumetric strains [69]. Interlamellar and intralamellar shear were nevertheless assumed to intervene as the strain increased owing to subsequent redistribution of the local stress through voiding and/or inhomogeneous stretching of the molecules in the amorphous layers, for example [3,4,10-14].

2D-WAXD patterns from the undeformed PA6TI and PA6TI-66 injection moldings (Figure 6d-e) provided further evidence for the anisotropic morphology implied by the SAXS results as well as significant molecular orientation along the specimen axes, the intensity distribution of the (h0k) reflections corresponding to the α structure of PA6TI indicating preferential orientation of the [010] direction parallel to the beam and preferential orientation of the normals to the (100) planes perpendicular to the specimen axes. The PA66 injection moldings were also textured (Figure 6f), with peaks in the intensity of the (100) reflections in the equatorial or near-equatorial positions and in the (002) reflections in the meridional or near-meridional positions, again indicating molecular orientation along the specimen axes and, in this case, preferential orientation of the [100] direction perpendicular to the specimen axes [70].

To access the influence of deformation on the crystal structure of the same specimens at room temperature, 2D-WAXD measurements were performed at different applied macroscopic strains. The resulting *in situ* 2D-WAXD patterns showed the crystallographic textures to strengthen in the plastically deformed regions of PA6TI-66 and PA66 as ε increased towards ε_f, indicating increased molecular orientation along the tensile axis (Figure 6d–f). By contrast, the patterns obtained from PA6TI changed little during straining owing to its relatively low ε_f and consequent limited plasticity under the experimental conditions associated with these measurements (Figure 6d). The d-spacings of the main Bragg reflections in PA6TI and PA66 either remained roughly constant or increased slightly with increasing ε (Figure 7, Supplementary Figure S4). As is usual in semicrystalline polymers, these increases followed the evolution of the macroscopic nominal

stress, σ, and were hence attributed to elastic deformation of the crystalline phase [71-73]. By contrast, the (001) peak in the terpolyamide PA6TI-66 broadened significantly in the strain range of 10–20 % corresponding to macroscopic yielding. At the same time, the PA6TI-66 (001) spacing increased sharply from its initial value of 12.3 Å to about 13.2 Å, and remained at this level for strains up to the effective ε_f of over 80 %. This increase in the PA6TI-66 (001) spacing was initially accompanied by a sharp decrease in the (100) spacing. However, the equatorial peaks again broadened at higher ε, and were progressively replaced by a single diffuse maximum at 2θ of about 21 ° at ε greater than about 40 % (Figure 7b and Supplementary Figure S4). We conclude from these observations that the terpolyamide PA6TI-66 underwent a strain-induced phase transformation on yielding, because of either crystallization of the initially amorphous regions or a crystal-crystal transformation in the deformed lamellae, or both.

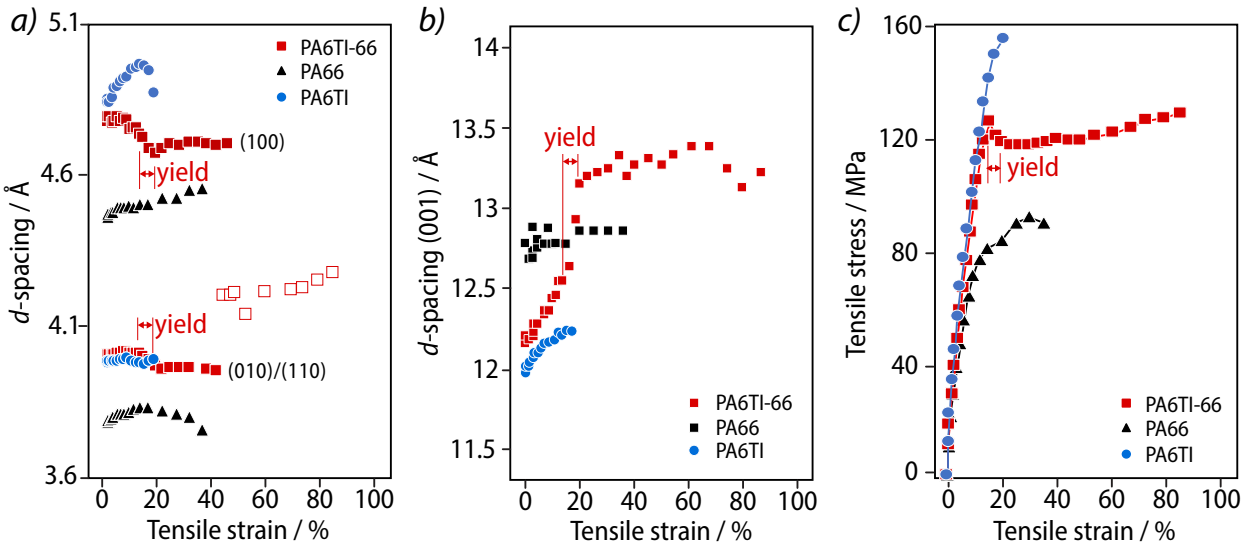

Figure 7. *a)* The (100) and (010) spacings (and the (110)/(010) spacings in the case of PA66) and *b)* the (001) spacings as a function of the macroscopic axial deformation of PA6TI, PA6TI-66, and PA66. In the corresponding nominal stress-strain curves given in *c)*, each stress value is the average of the stress measured during the recording of the diffraction pattern and the average nominal axial strain is estimated from the displacement of the specimen grips.

To gain further insight into the nature of these transformations, we compared the *d*-spacings of PA6TI-66 in the undeformed and deformed states with those of undeformed injection moldings of a series of PA6TI-PA66 terpolyamides with different aliphatic contents (Figure 8). This comparison is of interest because the dominant crystal structure of PA6TI-PA66 terpolyamides containing up to 40 *wt*% PA66, that is, up to the PA66 content of the PA6TI-66 terpolyamide that provided the focus for the present work, remains close to that of pure PA6TI, as a result of the isomorphous replacement of the T units in the crystalline PA6TI

domains with adipoyl units [35]. By contrast, the dominant crystal structure in the PA6TI-PA66 terpolyamides with compositions rich in PA66 (> 50 *wt*%) is a disordered form of the PA66 α structure incorporating a non-negligible concentration of aromatic units. In this latter regime, T_m consequently decreases monotonically with increasing PA6TI content, and the main *hk*0 spacings from undeformed specimens converge as the PA6TI content approaches 50 *wt*% (Figure 8a). Hence, although it is reported in the literature that isomorphous replacement of the PA66 adipoyl units by T units is possible in the PA66 α structure [74,75], this latter is clearly strongly perturbed by the presence of the aromatic units, which are too rigid to conform to the surrounding aliphatic units. The convergence of the main *hk*0 spacings in PA6TI-PA66 with increasing PA6TI content is reminiscent of the Brill transition (Figure 1b) but, in this case, the hydrogen-bonded planes were assumed to be forced apart by the presence of the rigid aromatic groups rather than increased mobility of the aliphatic segments.

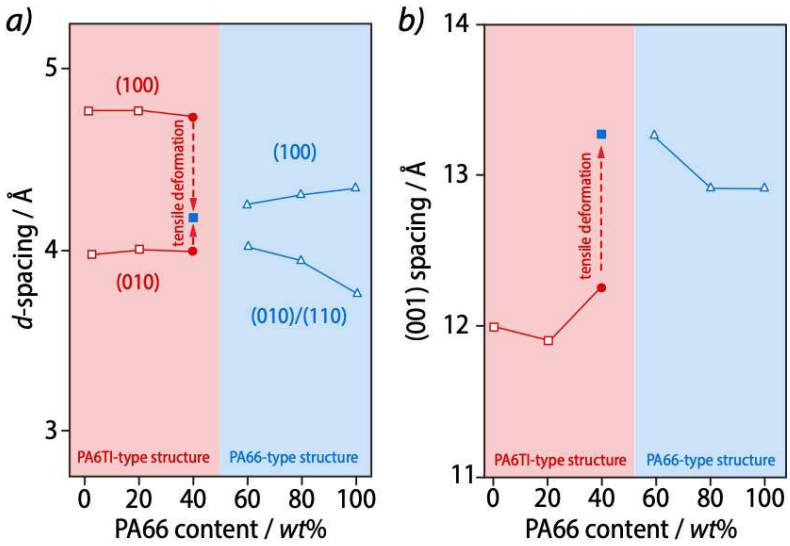

Figure 8. *a) d*-spacings corresponding to the main WAXD reflections and *b)* the implied (001) spacings as a function of PA66 content in PA6TI-PA66 terpolymers, together with the values measured in the *in situ* WAXD measurements for PA6TI-66 (PA6TI-40 wt% PA66) before (filled red symbols) and after (filled blue symbols) tensile deformation to strains greater than 40 % (cf. Figure 7).

The single diffuse *hk*0 peak that dominated the WAXD patterns for PA6TI-66 at large strains was therefore consistent with the presence of the disordered PA66 α structure, whose *hk*0 spacings may be inferred to converge fully at a PA66 content of 40 % (Figure 8a). This in turn implied more extended crystalline chain conformations in highly deformed in PA6TI-66 than in the undeformed specimens, although broadening of the WAXD peaks implied residual amounts of the PA6T α structure to persist even at large strains. The

formation of the disordered PA66 α structure during deformation of the initially amorphous regions despite the high overall PA6TI content may be rationalized as follows. Because an estimated 20 % of terephthaloyl units in the crystalline phase of PA6TI-66 are substituted by PA66 adipoyl units and the I units are assumed to be ejected from the crystalline regions [35], the observed SAXS degree of crystallinity of about 25 *vol*% implies the amorphous regions to contain 46 *wt*% PA66 units, 29 *wt*% PA6I units and only 31 *wt*% PA6T units.

Hence, the composition of the initially amorphous regions in PA6TI-66 is outside the range in which the PA6T α structure dominates in bulk moldings (Figure 8a). Indeed, deconvolution of the individual peaks (Supplementary Figure S4) suggested the disordered PA66 α structure may also have been present in the undeformed specimens of PA6TI-66. It was not possible to determine the relative proportions of the two phases quantitatively on this basis, owing to both the poor definition of the Bragg peaks and the contribution of oriented amorphous material to the equatorial scattering in the deformed specimens in the same range of scattering angles as the dominant hk0 reflections. However, the balance between the phases was strongly shifted towards the disordered PA66 α structure during yielding, and this trend continued at larger ε as plastic deformation propagated throughout the specimens.

The load-bearing capacity of voided deformation zones in polymers with respect to void growth and coalescence ultimately depends on that of the entanglement network, which was assumed to remain essentially intact after crystallization in the present case, given that the lamellar thicknesses were limited to 2–3 nm [35,76-78]. The lamellae provide a major, or even dominant contribution to the frictional forces that oppose disentanglement under stress in the solid state via forced reptation [79-81], which is known to dominate breakdown of the entanglement network in low T_g semicrystalline polymers such as polyethylene (PE) [82]. Moreover, strain-induced crystallinity has been observed directly in the initially amorphous regions of stretched thin films of PE and is consequently expected to make an important contribution to the exceptional ductility shown by many low T_g semicrystalline polymers [83].

The more limited mobility and higher stresses associated with deformation in the glassy state may nevertheless favor entanglement loss through chain scission of amorphous chain segments, that is, entangled strands and “tie molecules”, that are either initially stretched or become highly stretched during lamellar separation in the early stages of deformation [84-87]. Strain-induced crystallization of a partly

stretched network of flexible chains is well known to reduce entropic forces, leading to a more homogeneous distribution of load among the network strands [88-90]. It follows that strain-induced crystallization of the amorphous regions in PA6TI-66 should also contribute to the stability of the entanglement network with respect to void growth and coalescence at large deformations through chain scission. By contrast, again assuming the isophthaloyl units to be excluded from the crystalline phase, crystallization of the initially amorphous regions in unmodified PA6TI is likely to be very limited regardless of the extent of deformation.

Moreover, if deformation favors a more extended crystal conformation in the deformation direction, a crystal-crystal phase transformation may serve to relax the stresses on the intervening tie molecules, which might otherwise become very large in the absence of suitably oriented crystal slip systems. Direct estimates of the long period from SAED fiber patterns indicated the c-repeat distance of the disordered PA66 α phase to be about 17.2 Å. By contrast, the *c*-repeat distance was 16.42 Å in the PA6TI α structure, so that the observed deformation-induced phase transformation in PA6TI-66 was equivalent to a crystal strain of approximately 5 % in the chain direction. Relaxation may also be favored if the deformation-induced crystal phase is more mobile or if it constrains the amorphous material less than the PA6TI α phase lamellae. Certainly, in undeformed PA6TI and PA6TI-66 the PA6TI α phase lamellae are associated with a significant rigid amorphous fraction (RAF), whereas the presence of the disordered PA66 α phase in undeformed PA6TI-PA66 terpolymers with high PA66 contents is marked by a sharp decrease in the RAF [35]. This implies that a deformation-induced transition from the PA6TI α phase to the disordered PA66 α phase in PA6TI-66 may result in significantly increased mobility in the amorphous phase. Again, any such effects are unlikely to contribute to stress relaxation in unmodified PA6TI, in which the PA6TI α phase is always dominant.

Conclusions

In summary, we have provided strong evidence that yielding and the associated large deformations in the random terpolymer PA6TI-66 are accompanied by a phase transition from the α phase characteristic of unmodified PA6TI to a disordered form of the PA66 α phase in which the chain conformations are more extended, and which is suggested to be associated with the PA66-rich amorphous regions of the

undeformed specimens. This phase transition helps overcome what may be seen as a generic problem with semicrystalline copolymers that contain comonomers that do not participate in crystallization, such as the isophthaloyl (I) units in the case of PA6TI. By disrupting crystallization, the isophthaloyl units facilitate processing but, at the same time, compromise ductility because the isophthaloyl-rich amorphous regions are unable to crystallize even at large strains. By contrast, the PA6TI-66 random terpolyamide shows high degrees of tensile ductility and resilience over a wide range of temperatures. Moreover, although the crystalline phase in undeformed PA6TI-66 contains substitutional defects and its amorphous phase shows greater mobility than in PA6TI, both of which may facilitate plasticity, the degree of crystallinity and stiffness of PA6TI are largely maintained in PA6TI-66. This represents a significant advantage over previously described systems in which a metastable, low yield stress phase present in the undeformed polymer transforms to a more stable phase as the deformation increases. We have also evoked the possibility that a crystal-crystal transition to a phase associated with more extended chain conformations than in the undeformed PA6TI-66 may be effective in relaxing stresses on stretched amorphous chains that would otherwise lead to chain scission. Thus, changes in structure associated with yielding in PA6TI-66 may conceivably be associated with a pseudo- or super-plastic response in the crystalline regions, analogous to that observed in certain shape-memory alloys.

Finally, from a practical standpoint, the preparation of high-performance terpolyamides with enhanced ductility by simple melt-compounding has considerable potential for the replacement of metals in load-bearing structural parts in industrial applications that require high strength, stiffness and ductility, and in particular structural safety components whose role is to dissipate impact energy during collisions.

Materials and Methods

Melt Compounding

The starting materials, PA66 (M_n = 21'000 g/mol, M_w = 41'000 g/mol) and PA6TI (M_n = 12'000 g/mol, M_w = 24'000 g/mol), were provided by Ems Chemie AG and were dried for 1 h at 180 °C under vacuum and stored under vacuum before use. Extrusion processing was carried out using a co-rotating twin-screw micro-compounder with an integrated backflow channel (DSM Micro 5). The materials were circulated in the extruder for 12 min at 330 °C with a screw speed of 100 rpm. The molten material was then injected into a mold at 170 ° C with a hold time under pressure of about 20 s to give dog-bone specimens with a gauge length of 10 mm and a rectangular 1 × 2 mm^2 cross-section. All the specimens were again dried for 1 h at 180 °C under vacuum and then stored under vacuum prior to testing to avoid water uptake.

Dynamic Mechanical Analysis (DMA)

Dynamic mechanical testing (DMA Q800, TA Instruments) was performed in tensile mode with a strain amplitude of 10 μm, a frequency of 1 Hz and a preload of 1 N. The specimens were cooled to –140 °C and maintained at this temperature for 2 min. The measurements were then performed after successive increments of 5 °C in the temperature range –140 °C to 300 °C to give an overall heating rate of 3 °C/min. The test specimens were 1 × 2 × 10 mm^3 (thickness x width x length) bars prepared from the injection moldings.

Tensile Testing

The dog-bone specimens were tested using a universal testing machine (UTM, Walter+Bai) at a nominal strain rate of 5 % min^{-1}. The strain was measured using a clip-on extensometer with a gauge length of 10 mm. A minimum of five specimens were tested for each material. The Young's modulus was calculated from the limiting slope of the nominal stress-strain curve at zero strain.

Digital Image Correlation (DIC)

DIC was used to measure the 2D displacement field at the specimen surfaces from the evolution of a random speckle pattern obtained by applying white spray paint. A sequence of images of this pattern was recorded

during deformation using a stereovision system consisting of two Allied Vision Technologies Pike cameras (Supplementary Figure S2) in order to eliminate out of plane movement. The sampling rate was 2 Hz with a 50 ms exposure time that ensured a sufficiently low nominal strain increment between successive images. The images were post-processed using the VIC-3D software package (Correlated Solutions Inc.) to mesh a region of interest, ROI, at the specimen surface and hence track the speckle pattern during the test, as described in detail elsewhere [91]. At each macroscopic deformation step, the average longitudinal strain across the width of the specimen, ε_1, and the corresponding transverse strain, ε_2, were calculated at different points along the gauge length of the sample, with a spacing of 57μm (pixel size). The volumetric strain was then given by $\varepsilon_v = \varepsilon_1 + 2\varepsilon_2$, assuming transverse isotropy $\varepsilon_3 = \varepsilon_2$, where ε_3 is the through-thickness strain. Complementary measurements of the through-thickness strain field showed that $\varepsilon_3 = 0.90\ \varepsilon_2$, an effect attributed to transverse anisotropy induced by the molding process, suggesting an error of not more that 1 % in the volumetric strain calculated assuming $\varepsilon_3 = \varepsilon_2$. The high strain region of the specimen was then taken to correspond to measurement points for which ε_1 was greater than 80 % of the maximum measured value of ε_1. The average volumetric strain in these domains was then denoted ε_{vmax}.

Transmission Electron Microscopy (TEM)

Approximately 300 nm thick sections were prepared from the injection moldings using an ultramicrotome (LEICA EM UC7) and a diamond knife (Diatome Ultra 45°). Each section was deposited on a freshly cleaved KBr crystal and heated to 350 °C under nitrogen in a differential scanning calorimetry (DSC), held at 350°C for 2 min and cooled to ambient temperature at a cooling rate of 10 K/min. After recrystallization, the salt was dissolved in deionized water. The resulting film was then picked up on a roughly 1 x 2 mm^2 strip cut along the diagonals of a rectangular 100 mesh copper serial section TEM grid (Agar Scientific) and held at 270 °C for a few seconds to ensure adequate adhesion to the grid. The grid was then stretched manually at about 1 mm/s so that the film was deformed in uniaxial tension. The resulting damage zones were observed by TEM (TALOS F200X) in bright field with an accelerating voltage of 200 kV.

2D Wide-Angle X-Ray Diffraction (2D-WAXD) during Deformation

2D-WAXS patterns were recorded in transmission mode using a CCD Camera (Princeton Instrument) and a rotating anode X-Ray tube (CuKα, λ = 1.54 Å), a beam size of 500 × 500 μm^2 and a specimen-detector

distance of 42.1 mm. The transmission coefficient $\mu = 0.64\ mm^{-1}$ was determined from the intensity transmitted by specimens with different thicknesses assuming the Lambert-Beer law. Air scattering and direct beam intensities recorded in the absence of a specimen were subtracted from the total scattered intensity. Each scattering pattern was then integrated azimuthally to give 1D intensity profiles that were deconvoluted by fitting the crystalline and amorphous peaks with Lorentzian and Gaussian functions respectively. Mechanical tests were performed *in situ* using a miniature tensile test machine to stretch the specimen symmetrically so that the beam remained centered on its mid-point. A first WAXD pattern was recorded from the undeformed specimen, and the crosshead was then displaced in increments of at least 0.1 mm. After each increment, transient stresses were left to relax for 180 s before recording the WAXD pattern. The corresponding stress level was taken to be the average stress during the exposure time of 180 s. The overall test time therefore reached 2–3 hours for the most ductile specimens, which was two decades longer than the DIC tests, and plasticization effects due to water uptake may therefore have been significant. However, this did not lead to major qualitative changes in the mechanical behavior as borne out by the similarities in the stress-strain curves from the two types of test (Figure 7 and Figure 2a) despite the differences in the effective strain rate, indicating the materials behavior in all cases to remain representative of the glassy state.

1D Wide-Angle X-Ray Diffraction (1D-WAXD)

1D-WAXD patterns were measured using a Bruker D8 Advance spectrometer with non-monochromatic Cu radiation, a Göbel mirror and a 1D Lynxeye detector, equipped with a high temperature transmission furnace. 10 x 0.7 x 0.7 mm^3 strips were prepared from the injection moldings and loaded into 1.0 mm diameter quartz-glass capillaries. Temperature calibration was carried out using the equation of state of MgO and the acquisition time at each temperature was approximately 40 min.

Small-Angle X-Ray Scattering (SAXS)

The SAXS experiments were carried using the same rotating anode X-Ray tube as for the 2D-WAXD measurements with a specimen-detector distance of 343 mm and an exposure time of 1’200 s.

Acknowledgements

Funding from the Swiss *Kommission für Technologie und Innovation* (*KTI,* project 15503.1 PFIW-IW) is gratefully acknowledged. The authors would also like to thank the Interdisciplinary Electron Microscopy Center (CIME) of the EPFL for its technical assistance.

5. References

1. McCrum, N. G., Buckley, C. P., Bucknall, C. B., & Bucknall, C. B. 1997. Principles of polymer engineering. Oxford University Press, USA.
2. Biron, M. 2018. Thermoplastics and thermoplastic composites. 3rd edition. Elsevier.
3. Pawlak, A., Galeski, A. 2008. Cavitation during tensile deformation of polypropylene. Macromolecules 41, 2839–2851.
4. Pawlak, A., Galeski, A. 2014. Cavitation during deformation of semicrystalline polymers. Prog. Polym. Sci. 39, 921–958.
5. Boisot, G., Laiarinandrasana, L., Besson, J., Fond, C., Hochstetter, G. 2011. Experimental investigations and modeling of volume change induced by void growth in polyamide 11. Int. J. Solids Struct. 48, 2642–2654.
6. Laiarinandrasana, L. 2019. Stress heterogeneity leading to void nucleation within spherulites for semi-crystalline polymers. Crystals 9, 298.
7. Laiarinandrasana, L., Morgeneyer, T., Proudhon, H., N'Guyen, F., Maire, E. 2012. Effect of multiaxial stress state on morphology and spatial distribution of voids in deformed semicrystalline polymer assessed by X-ray tomography. Macromolecules 45, 4658–4668.
8. Ovalle, C., Cloetens, P., Proudhon, H., Morgeneyer, T. F., Laiarinandrasana, L. 2021. Nanocavitation mechanisms in deformed High Density Polyethylene (HDPE) using synchrotron radiation NanoTomography. Polymer 229, 123959.
9. Pawlak, A., & Galeski, A. 2005. Plastic deformation of crystalline polymers: the role of cavitation and crystal plasticity. Macromolecules, 38(23), 9688-9697.
10. Galeski, A. 2003. Strength and toughness of crystalline polymer systems. Prog. Polym. Sci. 28, 1643–1699.
11. Peterlin, A. 1971, Molecular model of drawing polyethylene and polypropylene. J. Mater. Sci. 6, 490-508.
12. Hiss, R., Hobeika, S., Lynn, C., Strobl, G. 1999. Network stretching, slip processes, and fragmentation of crystallites during uniaxial drawing of polyethylene and related copolymers. A comparative study. Macromolecules 32, 4390–4403.
13. Farge, L., Boisse, J., Dillet, J., André, S., Albouy, P.-A., Meneau, F. 2015. Wide-Angle X-ray Scattering Study of the Lamellar/Fibrillar Transition for a Semi-crystalline Polymer Deformed in Tension in Relation with the Evolution of Volume Strain, J. Polym. Sci. B Polym. Phys. 53, 1470–1480.
14. Humbert, S., Lame, O., Chenal, J. M., Rochas, C., Vigier, G. 2010. New Insight on Initiation of Cavitation in Semicrystalline Polymers: In-Situ SAXS Measurements. Macromolecules 43, 7212–7221

15. Xiong, B., Lame, O., Chenal, J. M., Men, Y., Seguela, R., Vigier, G. 2017. Critical stress and thermal activation of crystal plasticity in polyethylene: Influence of crystal microstructure and chain topology. Polymer 118, 192–200.
16. Plummer C.J.G., Kausch, H.-H., Deformation and entanglement in semicrystalline polymers. Journal of Macromolecular Science, Part B Physics 35, 1996, 637–657.
17. B. A. G. Schrauwen, R. P. M. Janssen, L. E. Govaert*, and H. E. H. Meijer, Intrinsic Deformation Behavior of Semicrystalline Polymers Macromolecules 2004, 37, 16, 6069–6078.
18. van Dommelen, J. A., Poluektov, M., Sedighiamiri, A., Govaert, L. E. 2017. Micromechanics of semicrystalline polymers: Towards quantitative predictions. Mechanics Research Communications 80, 4–9.
19. Kemmish, D. J. 2011. Practical guide to high performance engineering plastics, Ch. 3, Smithers Rapra, Shrewsbury, UK.
20. Fink, J. K., Partially aromatic polyamides, Second edition, p281, Elsevier, Amsterdam 2014.
21. Starkweather, H. W., Moore, G. E., Hansen, J. E., Roder, T. M., Brooks, R. E. 1958. Effect of crystallinity on the properties of nylons. J. Polym. Sci. 21, 189–204.
22. Starkweather, H. W., Brooks, R. E. 1959. Effect of spherulites on the mechanical properties of nylon 66. J. Appl. Polym. Sci., 11, 236–239.
23. Bucknall C. B., Heather, P. S., Lazzeri, A. 1989. Rubber toughening of plastics Part 12 Deformation mechanisms in toughened nylon 6,6. J. Mater. Sci. 16, 2255–2261
24. Ramsteiner, F., Heckmann, W. 1985. Mode of deformation in rubber-modified polyamide, Polym. Commun. 26, 199–200.
25. Wu, H., Krifa, M., Koo, J. H. 2018. Rubber (SEBS-g-MA) toughened flame-retardant polyamide 6: Microstructure, combustion, extension, and izod impact behavior. Polymer-Plastics Technology and Engineering 57, 727–739.
26. Plummer C. J. G., Mauger, M., Béguelin, P., Orange, G., Varlet, J. 2004. Fracture resistance of mineral reinforced PA6. Polymer 45, 1147–1157.
27. Penel-Pierron, L., Depecker C., Séguéla, R., Lefebvre, J.-M. 2001. Structural and mechanical behavior of nylon 6 films part I. Identification and stability of the crystalline phases. J. Polym. Sci. B Polym. Phys. 39, 484–495.
28. Pepin, J., Gaucher, V., Rochas, C., Lefebvre, J.-M. 2019. In-situ SAXS/WAXS investigations of the mechanically-induced phase transitions in semi-crystalline polyamides. Polymer 175, 87–98.
29. Penel-Pierron, L., Séguéla, R., Lefebvre, J.-M., Miri, V., Depecker C., Jutigny, M., Pabiot, J. 2001. Structural and mechanical behavior of nylon 6 films II. Uniaxial and Biaxial Drawing. J. Polym. Sci. B Polym. Phys. 39, 1224–1236.
30. De Rosa, C., Auriemma, F., de Ballesteros, O. R., Dello Iacono, S., De Luca, D., Resconi, L. 2009. Stress-Induced Polymorphic Transformations and Mechanical Properties of Isotactic Propylene-Hexene Copolymers. Cryst. Growth Des. 9, 165–176.
31. Auriemma, F., De Rosa, C., Di Girolamo, R., Malafronte, A., Scoti, M., Mitchell, G. R., Esposito, S. 2017. Deformation of stereoirregular isotactic polypropylene across length scales. Influence of temperature. Macromolecules 50, 2856–2870.
32. De Rosa, C., Auriemma, F. 2006. Structural-Mechanical Phase Diagram of Isotactic Polypropylene. J. Am. Chem. Soc., 128, 11024–11025.

33. Auriemma, F., De Rosa, C., Malafronte, A., Scoti, M. Di Girolamo, R. 2019. Solid state polymorphism of isotactic and syndiotactic polypropylene. In *Polypropylene Handbook*, Karger-Kocsis, J., Bárány, T. Eds., pp. 37–119, Springer Nature Switzerland, Cham.
34. Cretenoud, J., Galland, S., Plummer, C. J. G., Michaud, V., Bayer, A., Lamberts, N., Hoffmann, B., Frauenrath, H. 2017. High-temperature copolyamides obtained by the efficient transamidation of crystalline-crystalline polyamide blends, J. Appl. Polym. Sci. 134, 44349.
35. Candau, N., Galland, S., Cretenoud, J-M Chenal., O. Lame M., Balog, S., Michaud, V., Plummer, C. J. G., Frauenrath, H. 2021. High-Performance Polyamides with Engineered Disorder. Polymer Chemistry. DOI: 10.1039/D1PY01225H.
36. Miri, V., Persyn, O., Lefebvre, J. M., Séguéla, R. 2009. Effect of water absorption on the plastic deformation behavior of nylon 6. Eur. Polym. J. 45, 757–762.
37. Bunn, C. W., Garner, E. V. 1947. The crystal structures of two polyamides ('nylons'). Proc. Roy. Soc. A. 189, 39-68.
38. Brill, R. 1942, Über das Verhalten von Polyamiden beim Erhitzen, J. Prakt. Chem. 161, 49–64.
39. Brill, R. 1956, Beziehungen zwischen Wasserstoffbindung und einigen Eigenschaften von Polyamiden, Makromol. Chemie 18, 294–309.
40. Vasanthan, N., Murthy, N. S., Bray, R. G. 1998. Investigation of Brill Transition in Nylon 6 and Nylon 6,6 by Infrared Spectroscopy. Macromolecules 31, 8433–8435.
41. Xenopoulos, A., Wunderlich, B. 1991. Conformational motion and disorder in aliphatic nylons. The case of Nylon 6,6. Colloid Polym. Sci. 269, 375–391.
42. Lotz, B. 2021. Brill transition in nylons: the structural scenario. Macromolecules 54, 565–583.
43. Schmieder K., Wolf, K. 1953. Mechanische Relaxationserscheinungen an Hochpolymeren. Kolloid Z. 134, 148–189.
44. Park, Y., Ko, J., Ahn, T.-K., Choe, S. 1997. Moisture Effects on the Glass Transition and the Low Temperature Relaxations in Semiaromatic Polyamides. J. Polym. Sci. B Polym. Phys. 35, 807-815.
45. Bocahut, A., Delannoy, J.-Y., Long, D. R., Sotta, P. 2016. Modeling Molecular Relaxation Mechanisms in Amorphous Polymers: Application to Polyamides. Macromolecules, 49, 1918–1932.
46. Valles-Lluch, A. Camacho, , Ribes-Greus, A., Karlsson, S. 2002. Influence of water on the viscoelastic behavior of recycled nylon 6,6, J. Appl. Polym. Sci. 85, 2211-2218.
47. Bertoldo Menezes, D., Reyer, A., Marletta, A., Musso, M. 2016. Determination of the temperatures of the γ, β and α relaxation processes in nylon 6,6 by Raman spectroscopy, Polymer 106, 85–90.
48. Mourglia–Seignobos, E., Long, D. R., Odoni, L., Vanel, L., Sotta, P., Rochas, C. 2014. Physical mechanisms of fatigue in neat polyamide 6,6. Macromolecules, 47, 3880–3894.
49. Hoashi, K., Kawasaki, N., Andrews, R.D., Morphological Changes in Nylon 6 and Effect on Mechanical Properties IV. Stress-Strain Cycles in Structure and Properties of Polymer Films, Lenz R. W., Stein, R. S. Eds, p283, Plenum Press, New York 1973.
50. Humbert, S., Lame, O., Chenal, J. M., Rochas, C. & Vigier, G. 2010. New Insight on Initiation of Cavitation in Semicrystalline Polymers: In-Situ SAXS Measurements. Macromolecules 43, 7212–7221.
51. Castagnet, S., & Deburck, Y. (2007). Relative influence of microstructure and macroscopic triaxiality on cavitation damage in a semi-crystalline polymer. *Materials Science and Engineering: A*, *448*(1-2), 56-66.

52. Jeridi, M., Laiarinandrasana, L., Saï, K. 2014. Comparative study of continuum damage mechanics and Mechanics of Porous Media based on multi-mechanism model on Polyamide 6 semi-crystalline polymer. Int. J. Solid. Struct. 53, 12–27.
53. Tvergaard, V., Needleman, A. 1984. Analysis of the cup-cone fracture in a round tensile bar. Acta Methods Mater. 32, 157–169.
54. van Dommelen, J., Parks, D., Boyce, M., Brekelmans, W., Baaijens, F. 2003. Micromechanical modeling of the elasto-viscoplastic behavior of semicrystalline polymers. J. Mech. Phys. Sol. 51, 519–541.
55. Cayzac, H., Saï, K., Laiarinandrasana, L. 2013. Damage based constitutive relationships in semi-crystalline polymer by using multi-mechanisms model. Int. J. Plast. 51, 47–64.
56. Laiarinandrasana, L., Morgeneyer, T., Proudhon, H., Regrain, C. 2010. Damage of semicrystalline polyamide 6 assessed by 3D X-Ray tomography: from microstructural evolution to constitutive modeling. J. Pol. Sci. B/Polym. Phys. 48, 1516–1525.
57. Selles, N., Santier, N., Laiarinandrasana, L. 2016. Voiding mechanisms in semi-crystalline polyamide 6 during creep tests assessed by damage based constitutive relationships and finite elements calculations. Int. J. Plast. 86, 112–127.
58. Ovalle, C., Boisot, G., Laiarinandrasana, L. 2020. Effects of stress triaxiality ratio on the heat build-up of polyamide 11 under loading. Mechanics of Materials, 145, 103375.
59. Frank, F. I., Ruoff, A. L. 1958. A Method of Measuring Poisson's Ratio of Fibers. Text. Res. J. 28, 213–217.
60. Laiarinandrasana, L., Klinkova, O., Nguyen, F., Proudhon, H., Morgeneyer, T. F., Ludwig, W. 2016. Three dimensional quantification of anisotropic void evolution in deformed semi-crystalline polyamide 6. International Journal of Plasticity, 83, 19-36.
61. Lauterwasser, B. D., Kramer, E. J. 1979 Microscopic Mechanisms and Mechanics of Craze Growth and Fracture" Phil. Mag. A 39, 469-495.
62. Kramer, E. J. 1983 in Advances in Polymer Science: Microscopic and Molecular Fundamentals of Crazing, 52/53, Kausch, H.-H. Ed, p1, Springer, Berlin.
63. Galeski, A., Argon, A.S., Cohen, R.E. 1988. Changes in the morphology of bulk spherulitic nylon-6 due to plastic-deformation. Macromolecules 21, 2761–2770.
64. Detrez, F., Cantournet, S., Séguéla, R. 2011. Plasticity/damage coupling in semi-crystalline polymers prior to yielding: Micromechanisms and damage law identification. Polymer 52, 1998–2008.
65. Ferreiro, V., Pennec, Y., Séguéla, R., Coulon, G. 2001 Shear banding in polyamide 6 films as revealed by atomic force microscopy. Polymer 41, 1561–1569
66. More, A. P., Donald, A. M. 1992. The effect of metal halides on the deformation mechanism of thin films of nylon. Polymer 33, 4081–4086
67. Brandrup, J., Immergut, E. H., Grulke E. A. Eds. 2003. Polymer Handbook, 4th Edition, Wiley, New York.
68. Persyn, O., Miri, V., LeFebvre, J.-M., Ferreiro, V., Brink, T., Stroeks, A. Mechanical Behavior of Films of Miscible Polyamide 6/Polyamide 6I-6T Blends. J. Polym. Sci. B Polym. Phys. 44, 1690–1701.
69. Butler, M. F., Donald, A. M., Ryan, A. J. 1998. Time resolved simultaneous small-and wide-angle X-ray scattering during polyethylene deformation–II. Cold drawing of linear polyethylene, Polymer 39, 39–52.

70. Lovinger, A. J. 1978. Crystallographic factors affecting the structure of polymeric spherulites. II. X-ray diffraction analysis of directionally solidified polyamides and general conclusions. Journal of Applied Physics 49, 5014-5028.
71. Sakurada, I., Nukushina, Y., Ito, T. 1962. Experimental determination of the elastic modulus of crystalline regions in oriented polymers. Journal of Polymer Science 57, 651–660.
72. Xiong, B., Lame, O., Chenal, J. M., Rochas, C., Seguela, R., Vigier, G. 2015. Amorphous phase modulus and micro–macro scale relationship in polyethylene via in situ SAXS and WAXS. Macromolecules 48, 2149–2160.
73. Xiong, B., Lame, O., Seguela, R., Men, Y. 2018. Micro/macro-stress relationship and local stress distribution in polyethylene spherulites upon uniaxial stretching in the small strain domain. Polymer 140, 215–224.
74. Edgar, O. B.; Hill, R. 1952. The p-phenylene linkage in linear high polymers: Some structure–property relationships. J. Polym. Sci. 8, 1–22
75. Harvey, E. D., Hybart, F. J. 1971. The melting and crystallization of copolymers of nylon-6,6 and nylon-6,10 with poly(hexamethylene terephthalamide) (Nylon–6T). Polymer 12, 711–716.
76. Flory, P. J., Yoon, D Y. 1978. Molecular morphology in semicrystalline polymers, Nature 272, 226–229,
77. Guenet, J.–M. 1981. Neutron scattering investigations on the effect of crystallization temperature and thermal treatment on the chain trajectory in bulk-crystallized isotactic polystyrene. Polymer 22, 313–320.
78. Plummer, C. J. G., Cudre-Mauroux, N., Kausch, H.-H. 1994. Deformation and entanglement in semicrystalline polymers, Polym. Eng. Sci. 34, 318–329.
79. McLeish, T. C. B., Plummer, C. J. G., Donald, A. M. 1989. Crazing by disentanglement: non-diffusive reptation. Polymer 30, 1651–1655.
80. Plummer, C. J. G., Kausch, H.-H. 1993. Deformation of thin films of poly(ether ether ketone), Polymer 34, 305–311.
81. Gensler, R., Plummer, C. J. G., Kausch, H.-H., Munstedt, H. 1997. Thin film and bulk deformation behaviour of poly(ether ether ketone)/poly(ether imide) blends, J. Mater. Sci. 32, 3037–3042.
82. Bartczak, Z., Grala, M., Richaud, E., Gadzinowska, K., 2016. Erosion of the molecular network in the amorphous layers of polyethylene upon high-strain deformation. Polymer 99, 552–565.
83. Wade Adams, W., Yang, D., Thomas, E. L. 1986. Direct visualization of microstructural deformation processes in polyethylene. J. Mater. Sci. 21, 2239–2253.
84. Huang, Y.-L., Brown, N. 1988. The effect of molecular weight on slow crack growth in linear polyethylene homopolymers. J. Mater. Sci. 23, 3648–3655.
85. Yeh, J. T., Runt, J. 1991. Fatigue crack propagation in high-density polyethylene. J. Polym. Sci. B. Polym. Phys. 29, 371–388.
86. Séguéla, R. 2005. Critical Review of the Molecular Topology of Semicrystalline Polymers: The Origin and Assessment of Intercrystalline Tie Molecules and Chain Entanglements. J. Polym. Sci. B Polym. Phys. 43, 1729–1748.
87. DesLauriers, P.J., Lamborn, M. J., Fodor, J. S. 2018. Correlating polyethylene microstructure to stress cracking; correlations to post yield tensile tests. Polymer 153, 422–429.
88. Toki, S., Che, J., Rong, L., Hsiao, B. S., Amnuaypornsri, S., Nimpaiboon, A., Sakdapipanich, J. 2013. Entanglements and Networks to Strain-Induced Crystallization and Stress–Strain Relations in Natural Rubber and Synthetic Polyisoprene at Various Temperatures. Macromolecules 46, 5238–5248.

89. Tosaka, M., Kohjiya, S., Ikeda, Y., Toki, S., Hsiao, B. S. 2010. Molecular orientation and stress relaxation during strain-induced crystallization of vulcanized natural rubber, Polym. J., 42, 474–481.
90. Candau, N., Chazeau, L., Chenal, J. M., Gauthier, C. and Munch, E. 2016. Complex dependence on the elastically active chains density of the strain induced crystallization of vulcanized natural rubbers, from low to high strain rate. Polymer 97, 158–166.
91. Candau, N., Pradille, C., Bouvard, J. L., & Billon, N. (2016). On the use of a four-cameras stereovision system to characterize large 3D deformation in elastomers. *Polymer Testing*, *56*, 314-320.